

A Microphone Array on a Chip for High Spatial Resolution Measurements of Turbulence

Joshua S. Krause, Judith M. Gallman, Mark J. Moeller, and Robert D. White, *Member, IEEE*

Abstract—A microelectromechanical systems-based microphone array on a chip has been developed and applied to aeroacoustic measurements. The array is designed to measure the fluctuating pressures present under a turbulent boundary layer (TBL). Each chip measures 1 cm^2 and contains 64 individually addressable capacitively sensed microphones, with a center to center pitch of $\sim 1.25 \text{ mm}$. Surface topology, including the packaging, is kept to less than 0.13 mm . Element-to-element sensitivity variation in the array is less than $\pm 2.5 \text{ dB}$ from least to most sensitive, and phase variation is less than $\pm 6.5^\circ$ (at 1 kHz). The microphone 3-dB bandwidth is 700 Hz to 200 kHz , and the microphones are linear to better than 0.3% at sound pressure levels up to 150-dB SPL . A unique switched architecture system electronics and packaging method are employed to reduce data acquisition channel count requirements, and to maintain a low surface roughness. The array has been applied to the measurement of single point turbulence spectra under a flat plate TBL in a flow duct at Mach numbers up to 0.6 and Reynolds numbers based on plate length of 10^7 . [2013-0013]

Index Terms—Microphone, turbulence, array, sensor, pressure, aeroacoustic.

I. INTRODUCTION

PRESSURE fluctuations beneath the turbulent boundary layer (TBL) are one of two primary sources of externally radiated noise in aircraft (the other being engine noise). The internal cabin noise in aircraft is also generated primarily by a combination of TBL pressure fluctuations and engine noise, with an additional component coming from environmental air handling systems. In order to design the aircraft structure to reduce internal and external noise generated by TBL pressure fluctuations, high fidelity characterization of the wall pressure spectrum in spatial wavenumber space and in temporal frequency is needed. The wavenumber/frequency pressure spectra is the forcing function which sets up structural vibrations in the aircraft body, leading both to re-radiated external noise and radiation into the inside of the aircraft.

Manuscript received January 8, 2013; revised January 8, 2014; accepted February 2, 2014. Date of publication March 31, 2014; date of current version September 29, 2014. Subject Editor R. Maboudian.

J. S. Krause was with the Mechanical Engineering Department, Tufts University, Medford, MA 02155 USA. He is now with Integrated Defense Systems, Andover, MA 01810 USA (e-mail: joshua.s.krause@raytheon.com).

J. M. Gallman was with Spirit Aerosystems, Inc., Wichita, KS 67278 USA. She is now with Gulfstream Aerospace Corporation, Savannah, GA 31402 USA (e-mail: judith.gallman@gulfstream.com).

M. J. Moeller was with Spirit Aerosystems, Inc., Wichita, KS 67278 USA. He is now an independent Noise and Vibration Consultant (e-mail: mark.j.moeller@spiraero.com).

R. D. White is with the Mechanical Engineering Department, Tufts University, Medford, MA 02155 USA (e-mail: r.white@tufts.edu).

Color versions of one or more of the figures in this paper are available online at <http://ieeexplore.ieee.org>.

Digital Object Identifier 10.1109/JMEMS.2014.2307556

Turbulent surface pressure measurements taken in the past [1]–[5] have been limited by the large size and limited array aperture of the transducers. In particular, traditional sensors are too large to measure the small-scale fluctuations under the TBL, resulting in spatial averaging as well as a low pass temporal filter characteristic [6]. This leads to a loss of information at high wavenumbers and high frequencies. By moving to smaller MEMS sensors and larger arrays, an increase in spatial and temporal resolution can be obtained [7]. In addition, MEMS microphones have high bandwidth and high dynamic range, both of which are needed for TBL measurements. To date, arrays of either MEMS or traditional microphones that have been applied to TBL measurements have been limited to 4 to 24 element arrays, with minimum spacing on the order of 5 mm (e.g. Blake and Chase, Farabee and Geib, Bhat, Berns, *et al*, Arnold, *et al* [2], [3], [8]–[10]). In the current work a microphone array on a chip is described which consists of 64 elements, with a center-to-center pitch of 1.26 mm in the flow direction, and 1.11 mm in the cross-flow direction. This is the largest MEMS microphone array employed to date for TBL measurements, and is the only example in the literature of an addressable microphone array on a single chip, with the advantages of fine element pitch and reduced interconnect complexity. Initial work in the design of this system was published in conference proceedings by the authors. The full system is described in this paper [11]–[14].

The purpose of the device was to investigate the wavenumber frequency spectrum as it would apply to predicting interior noise in aircraft. We were specifically looking for Mach dependence at high subsonic Mach numbers. The particular flow facility that was targeted limited experimental work to Mach 0.6 . For our boundary layer, packaging topology limited the useful frequency range for the array to low and midfrequency. In terms of the wall pressure that could be measured, sources would be due to the wake and the log overlap region of the boundary layer, again further out than the viscous sublayer. In particular, the array was designed to help answer questions about the two dimensionality of the flow; specifically how the wall pressure was distributed in the cross stream direction. One of the planned uses was to investigate the Mellen conjecture, that a separable flow model was not representative of the wall pressure [44]–[46]. In addition, although in this work the array chip is only 1 cm in extent, the chip was designed such that the pitch would be maintained when multiple chips were assembled in a line. This opens up the possibility of future experiments using multiple chips to investigate the larger scale features of the boundary layer.

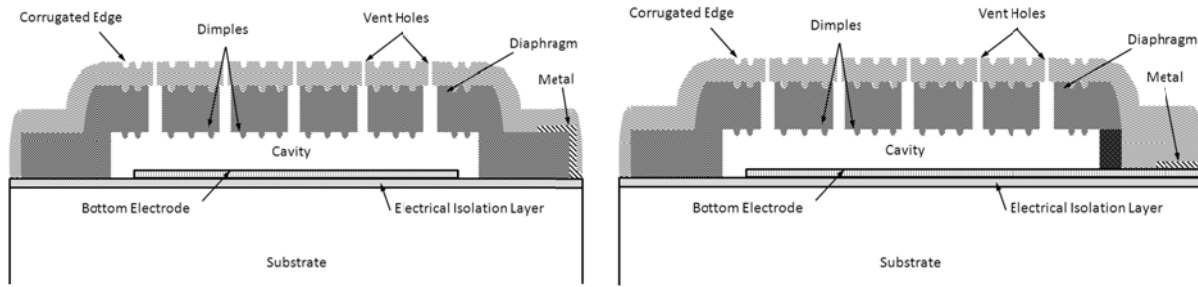


Fig. 1. Schematic of one element in the microphone array showing two cross-sectional views at two angular cuts.

In order to determine the targets for a TBL measurement system, we consider flow speeds typical of commercial aircraft, and also relevant to the available flow testing facility. At Mach 0.4 to Mach 0.9 at 3 meters down a flat plate, the Reynolds number based on plate length is on the order of $Re_L = 10^7$, and thus the velocity boundary layer thickness is expected to be approximately $\delta = 3$ to 5 cm [15], [16]. This is computed based on a $1/7^{\text{th}}$ power law approximation. The smallest scales of turbulence are at the Kolmogorov length scale, which for these same parameters is approximately $5 \mu\text{m}$ [16]–[18]. Single point wall spectral models for pressure suggest that temporal frequencies up to 200 kHz will carry significant energy [16]–[18]. Thus, ideally, microphone arrays applied to TBL sensing under these conditions should be 3 to 5 cm in total extent with spatial resolution of $5 \mu\text{m}$, bandwidth greater than 200 kHz, and a dynamic range of 160 dB SPL in pressure. The array described in this work achieves the desired dynamic range and bandwidth, and takes steps towards reaching the ultimate goal of spatial resolutions below $10 \mu\text{m}$. In particular, the system described here achieves a pitch of 1.1 to 1.3 mm, approximately 5 times finer than any previously described aeroacoustic microphone array.

In order to operate easily in both ground testing environments and potentially in flight testing environments, it is helpful to front vent the microphone. This allows the static pressure to equalize across the diaphragm to the pressure inside the tunnel (in ground testing) or to atmosphere (in flight testing). Front venting is achieved with the current microphone by including small holes in the diaphragm. Controlling the size of these holes is critical to recovering the low frequency sensitivity of the device, as will be described in the paper, but can be successfully achieved using high resolution micromachining techniques, which allow the hole size to be controlled to better than 1 micron precision.

An additional concern for this type of measurement is that, when large numbers of small sensors are used, packaging and data processing become challenging. Electronics are needed for signal routing and amplification, and data must be acquired without unrealistically large channel counts. In addition, the sensor arrays must be conformally packaged with a surface roughness that is less than the viscous sublayer thickness in order to not disturb the flow. For these conditions, the viscous sublayer is on the order of $20 \mu\text{m}$. Thus, in this work, we emphasize a systems approach to aeroacoustic MEMS microphone design. In addition to the design of the individual sensor elements, the entire system will be considered,

including system level electronics, and packaging technologies for low profile arrays.

II. DESIGN AND MICROFABRICATION

The individual elements of the array are capacitively sensed microphones with a $3.5 \mu\text{m}$ thick, $600 \mu\text{m}$ diameter polysilicon diaphragm separated from the backing electrode by a $2 \mu\text{m}$ air gap. The polysilicon diaphragm is coated with a $2 \mu\text{m}$ thick Parylene C layer. A cross sectional diagram of an individual element is shown in Fig. 1. In the first cross-section, the cavity, diaphragm, and bottom electrode are seen. In the second cross-section, which is along a different angular cut, the region where the metal trace “tunnels” under the diaphragm anchor, surrounded by an insulating oxide, can also be seen. The dimples, vent holes, and corrugated edges are also shown in Fig. 1.

The fabrication of the microphone chip was conducted using the MEMSCAP PolyMUMPs® process [MEMSCAP, NC] along with facilities at Tufts University’s Micro and Nano Fabrication Facility. The PolyMUMPs® process is a foundry process that produces polysilicon structures via surface micromachining with a minimum feature size of $2 \mu\text{m}$. The process deposits seven physical layers, including three structural, two sacrificial and one metal interconnect layer. The process is established and has been discussed in literature for over twenty years [19], [20]. The chip described in this paper was fabricated in PolyMUMPS Run 86.

Fig. 2 illustrates each step in the fabrication process. The substrate was a silicon wafer with a 600 nm layer of silicon nitride deposited by LPCVD. The second layer was a 500 nm heavily phosphorous doped polysilicon layer, which provided the bottom electrode in the capacitive microphone scheme. The shape of the electrode was a disc with a diameter of $580 \mu\text{m}$. The bottom electrode also had a “tunneling region” where the polysilicon structure extends out from the disk to connect the electrode to the biasing connections. To prevent a short between bottom and top electrode, the tunneling region extended under the diaphragm supports using the sacrificial oxide as insulation from the top electrode. Following the first polysilicon layer, the $2 \mu\text{m}$ thick sacrificial layer (phosphosilicate glass, PSG) was deposited and patterned. This layer was removed during the sacrificial etch and create the backing cavity between the diaphragm and bottom electrode. Two additional features were created by dry etching the sacrificial oxide to a depth of 750 nm . This is the DIMPLE layer in the PolyMUMPS process, and produces surface features in

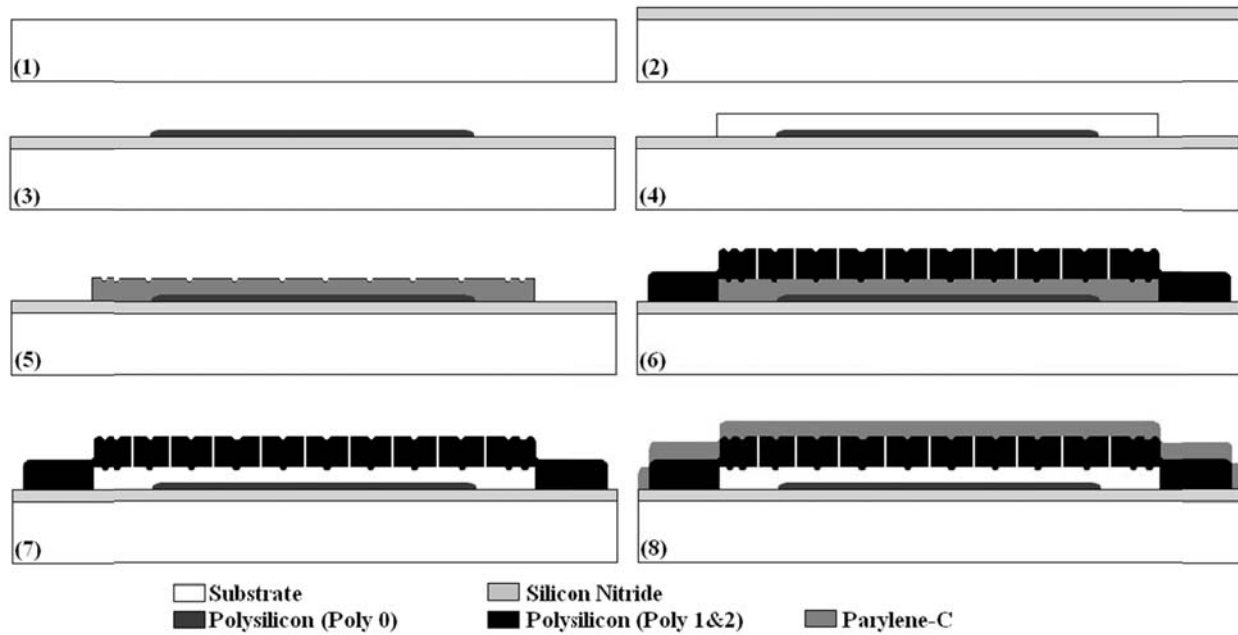


Fig. 2. Schematic illustrating the array chip fabrication process. Steps (1)–(6) are the MEMSCAP PolyMUMPS[®] process. Steps (7) and (8) were conducted in post processing. (1) Bare silicon substrate, surface heavily doped with phosphorus. (2) Silicon Nitride layer is deposited as an electrical isolation layer. (3) Bottom electrode is patterned in the Poly 0 layer. (4) Sacrificial oxide layer is deposited to create the cavity. (5) Dimples and corrugations are patterned into the 1st Oxide layer. (6) Poly 1 and Poly 2 layers are deposited as the diaphragm. (7) Sacrificial oxide is removed using a 4:1 HF:HCl release. (8) Parylene-C is deposited to protect the surface and control vent hole diameter.

TABLE I
GEOMETRIC PROPERTIES OF THE MICROPHONE

Symbol	Property	Value	Units
a	Radius of the diaphragm	300	μm
t_1	Thickness of polysilicon layer	3.5	μm
t_2	Thickness of Parylene-C layer	2	μm
g_0	Gap height (sacrificial layer thickness)	2	μm
a_{hole}	Radius of diaphragm vent holes	≈ 1	μm
n	Number of vent holes in diaphragm	28	-

the polysilicon structure. Four micron diameter dimples were spaced $30 \mu\text{m}$ apart in a square grid pattern across the structure. The dimples help to reduce stiction, a common problem in the release of MEMS structures. The spacing of the dimples was selected through the use of the peel number calculations and the approximation that the structure between dimples acts similarly to a doubly supported beam, [21]. The dimple mask was also used to fabricate two circular corrugations close to the edge of the diaphragm. This allowed for the partial relaxation of residual stresses inherent in the fabrication of the diaphragm. The reduction of residual stress may have the additional benefit of a slight increase in sensitivity during

operation [22]. Various geometric parameters for the design are given in Table I.

The second and third polysilicon layers (also heavily doped) were combined to create a $3.5 \mu\text{m}$ thick diaphragm (top electrode) with a diameter of $600 \mu\text{m}$. A final feature of note is the vent holes which are etched through the polysilicon diaphragm. They serve two purposes. First, these holes are used to introduce the wet etchant to remove the PSG sacrificial layer. Second, the holes act as “frontside” vents to equalize ambient pressure with gap pressure. Finally, they can be used to control damping to set the low frequency response of the microphone. This is a critical feature of the

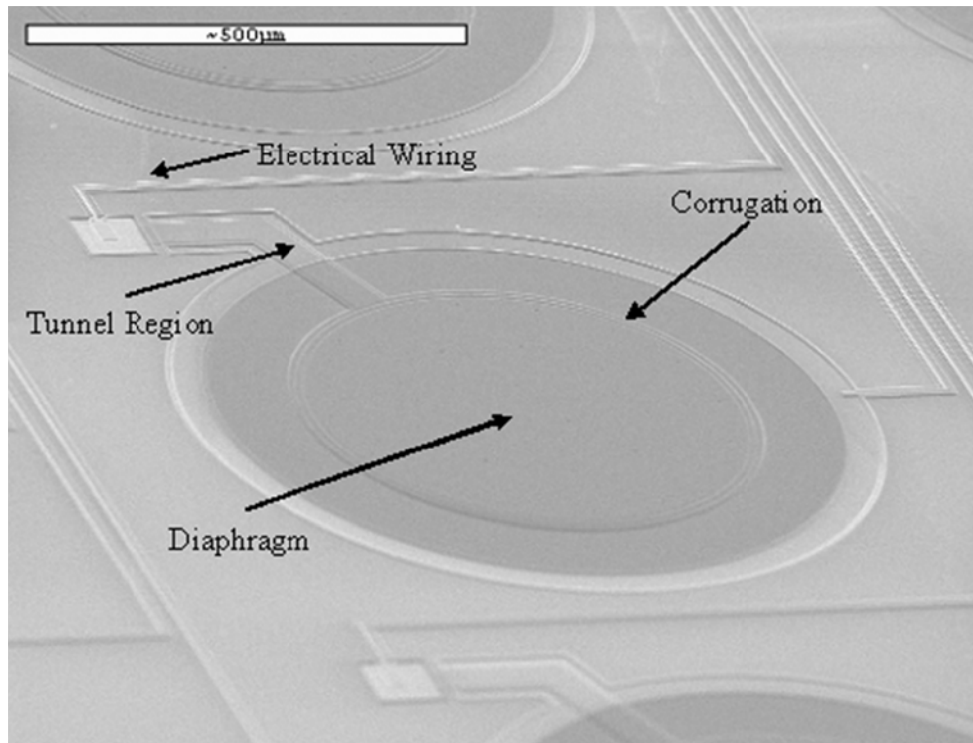


Fig. 3. SEM image of an element illustrating the diaphragm, corrugation around diaphragm, wire scheme, and tunnel concept for electrical connection to bottom electrode. The diaphragm diameter is $600 \mu\text{m}$.

design. After patterning of the polysilicon structural layer, the polyMUMPS portion of the fabrication process was completed by depositing, via evaporation, and patterning, via liftoff, a 500 nm thick gold layer with a thin chromium adhesion layer. This metal layer was used to create the electrical connections and bond pads for all the array elements. All the wires and pads were created out of a laminate of doped polysilicon and metal, anchored directly to the nitride layer or to the bulk silicon, as appropriate. The final design implemented grounded guard bands in between each pair of signal lines to reduce cross talk between channels. Fig. 3 shows a scanning electron microscope (SEM) image of an individual microphone in the array illustrating many of these design features.

The microphones were arrayed on a $1.01 \text{ cm} \times 1.01 \text{ cm}$ chip in an 8×8 pattern. There were 72 bond pads along two edges of the chip for electrical connection. During operation, the direction of flow was parallel to the bond pads, to minimize the impact of the wirebonds on the flow. The microphone center-to-center spacing in the direction of flow was 1.2625 mm (which allowed for multiple 8×8 arrays to be placed end-to-end to determine low wavenumber information through the larger spatial scale), while the pitch across the flow was 1.1125 mm (necessitated by the bonding pads). A photograph of a microphone array chip after the PolyMUMPS process is shown in Fig. 4.

III. RELEASE AND PACKAGING

The release etch was conducted after the chips were returned from the PolyMUMPS process. Release consisted of a 45 minute, 4:1 hydrofluoric acid (49% HF) to hydrochloric acid (HCl 37%) etch. The mixture of HF and HCl was used

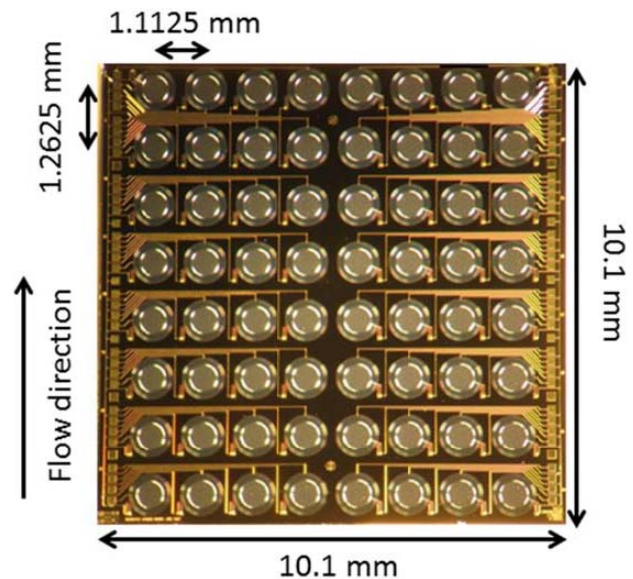


Fig. 4. Photograph of the microphone array chip after microfabrication is complete but before the release etch or packaging process.

due to the reduction in the electrochemical effect between the metal layer and the polysilicon structures by adding the HCl rather than undiluted (49%) HF. It was demonstrated by Miller *et al.* that the galvanic corrosion of the grain boundaries in the doped polysilicon can be reduced by using a 4:1 HF:HCl mixture [23]. Results of chip testing in this work clearly indicated that including the HCl in the etch substantially reduced galvanic corrosion, as measured by the considerable reduction in resistance of the polysilicon interconnects.

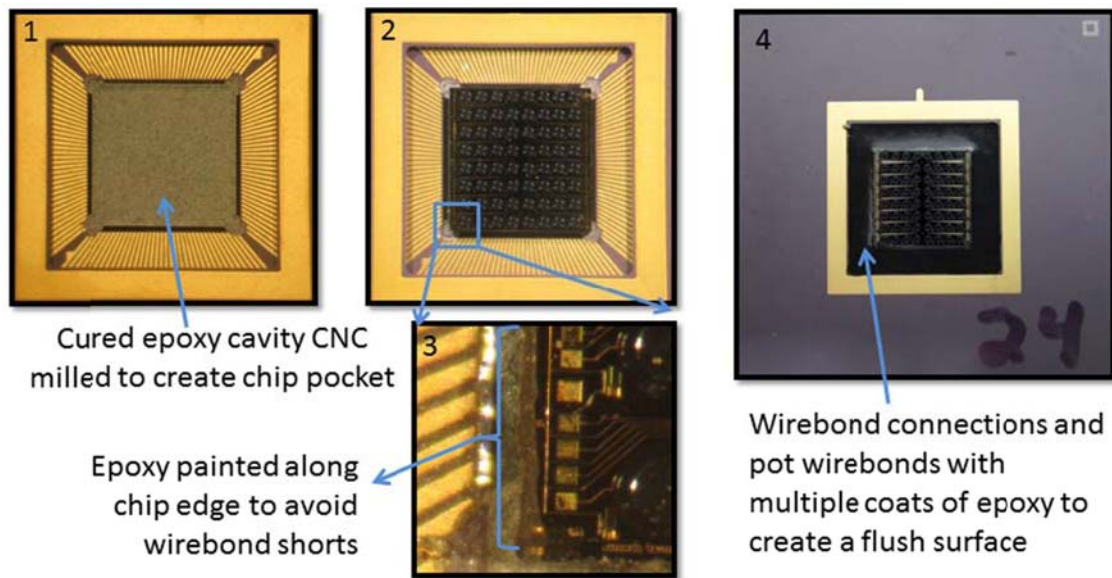


Fig. 5. Photographs showing the steps in the packaging process. (1) The CPGA cavity is filled with epoxy, cured, and CNC milled to produce a pocket for the chip. (2) The chip is placed and bonded in with a thin epoxy. (3) Epoxy is painted along the edge of the chip to avoid wirebond shorts to the silicon corner. (4) Connections are ball bonded and the cavity filled with potting epoxy.

After the etch of the sacrificial oxide, the arrays were placed in a bath of 1:4 methanol to deionized water for 15 minutes to remove and dilute any residual HF and then undiluted methanol for 15 minutes to reduce the amount of surface tension when drying. When the arrays were removed from the methanol bath, they were dried in a dry air container at 20 percent relative humidity. It was found that by using a reduced relative humidity during drying, stiction of the diaphragms could be reduced. When this system was in place, the release of the microphone array had 100 percent yield from the microphone sticking down as tested by the resistance and capacitance between the top and bottom electrodes.

Packaging used a ceramic pin grid array (CPGA), in which the MEMS array was epoxied, wirebonded, and potted. Photographs illustrating the steps in the process are shown in Fig. 5. The CPGA cavity was first partially filled with a high resistivity ($3 \cdot 10^{13} \Omega\text{-cm}$), low thermal expansion ($15 \text{ ppm}/^\circ\text{C}$) potting epoxy [Namics Chipcoat G8345-6]. This epoxy is chosen to more closely match the thermal coefficient of expansion of the silicon chip ($3 \text{ ppm}/^\circ\text{C}$), in order to minimize the effects that a change in temperature could have on the silicon chip. The epoxy was deposited in the center of the CPGA, so that it would cure at a position above the finger bonds. After a two hour, $90^\circ\text{C}/160^\circ\text{C}$ cure, the epoxy was milled flat and a square pocket was milled out, using a CNC milling machine. The pocket was sized to center and square the chip, as well as position it at the required height so it would be planar with the top of the CPGA, as shown in Fig. 5 step 1.

A thin layer of epoxy was placed into the cavity, the chip was placed on top, and a ball bonding machine was used to apply 80 grams of force onto the center of the chip to ensure that it was flush and well bonded. The epoxy was cured at 90°C for one hour, followed by 160°C for one hour, resulting in the structure shown in Fig. 5 step 2. It was found that a low CTE epoxy such as the Namics Chipcoat G8345-6 was needed

to avoid inducing thermal stresses into the MEMS array which could buckle the membranes. As shown in Fig. 5 step 3, very thin strip of epoxy was hand painted onto the edge of the chip using a small probe in order to coat the corner; this was found to reduce the number of short circuits created between the wirebonds and the backside silicon as they loop over the chip edge at a low angle. The chip was then electrically ball bonded to the package using 25 micron diameter gold wire. Care was taken to keep the wirebond profile as low as possible.

The penultimate step in the packaging process was the deposition of an approximately $2 \mu\text{m}$ thick layer of Parylene (Poly-para-xylylene) type C via chemical vapor deposition. The Parylene-C acts as an electrical isolation layer, covering the wirebonds, connection terminals on the CPGA, as well as the diaphragms and all other parts of the chip surface. It is postulated that this will produce a more robust device that could withstand greater environmental effects, most notably resistance to moisture, although moisture resistance has not been explicitly tested. A second important role for the Parylene C is control of the vent hole diameter. The chip is acoustically calibrated, as described below, and then additional thickness of Parylene is deposited, followed by more acoustic testing. The process is repeated until the low frequency sensitivity of the chip is recovered to approximately 500 Hz, demonstrating that the vent holes have been sufficiently closed up but not sealed. After Parylene deposition, the wirebonds were covered in the Chipcoat potting epoxy, and the area around the chip filled. Multiple coats were used and cured (2 hours $90^\circ\text{C}/160^\circ\text{C}$) in order to achieve a flat surface from the CPGA ceramic, onto the potting epoxy, and onto the surface of the MEMS chip. The final resulting packaged chip is shown in step 4.

Surface profile measurements across these three regions are given below. This surface profile was critical for flow

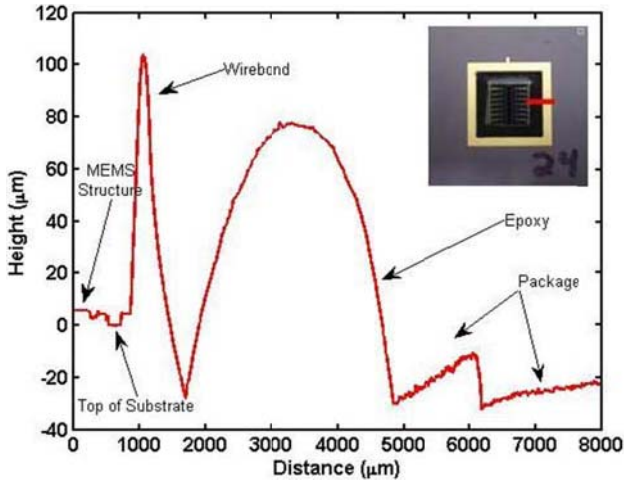


Fig. 6. Measured surface topology after packaging.

testing. If the chip was recessed in a depression or protruded significantly above the wind tunnel wall, this would cause unwanted flow alterations (either decreased pressure fluctuations due to flow separation over the array or an increase in turbulence not associated with TBL flow characteristics). The surface topology from the microphones, die, wirebonds, potting epoxy and chip is shown in Fig. 6 (with inset picture indicating measurement location in red). The measurements show that the height difference from the package to the die is 25 microns, which is less than the viscous sublayer thickness and should cause minimal flow disturbance. However, the topology between the package and the top of the wirebonds is close to 125 microns. This is larger than desired and could lead to some flow disturbance. Indeed, work on intentionally modifying surfaces with regular microscale “riblets” on the order of 10 wall units in height (approximately 50 microns for the flow problem under consideration) show drag reductions on the order of 10% [43]. Hence, it is desirable to further reduce packaging topology. However, the problem is mitigated in this work by directing the flow lengthwise along the chip so that it does not pass over the 125 micron high wirebonds. Nevertheless, if improvements can be made to the packaging process in the future to avoid the use of frontside wirebonds, perhaps by thin film interconnect on the frontside to through silicon vias and backside bump connections, it would be beneficial.

IV. SYSTEM ELECTRONICS

Board level electronics were used for the system, as diagrammed in Fig. 7. A precision 10V reference IC, ADR01 [Analog Devices, Wilmington, MA] provides a DC bias to all the MEMS microphones via the bottom electrode. Each microphone output, coming from the top (diaphragm) electrode, is fed into three CMOS switches [ADG714, Analog Devices, Wilmington, MA]. These switches allow the microphone signal to be sent to one of two preamplifier channels, or to ground. It is emphasized that more than one microphone can be switched on at a time; due to the charge integrating nature of the preamplifier, switching multiple microphones to

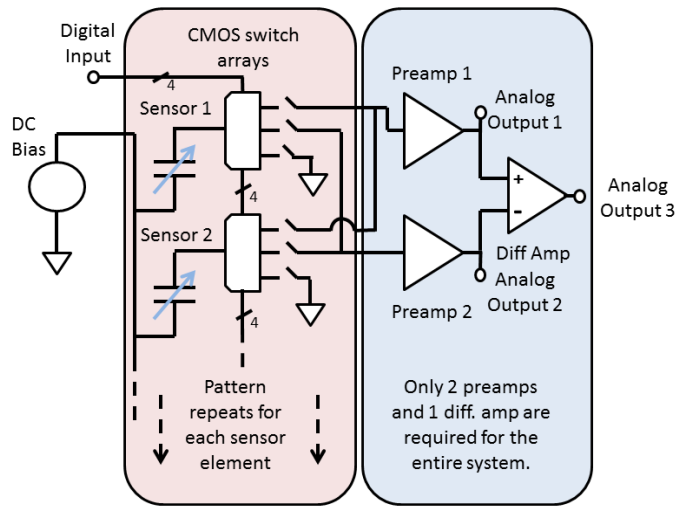


Fig. 7. Schematic of the system electronics. Each MEMS sensor feeds three CMOS switches, which allow the sensors to be switched to pre-amplifier #1, #2 or to ground.

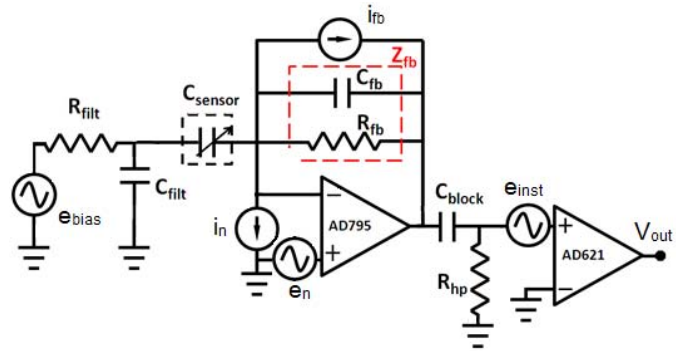


Fig. 8. A detailed circuit model of the bias source, preamplifier, and differential amplifier, showing all major noise sources.

the same preamplifier causes their outputs to sum. The selected microphones act together in parallel. This allows the individual microphones to be turned on and off via serial computer control and can create different array patterns on the fly. Computer control of the CMOS switches is managed by a computer communicating to the CMOS chips via a Labview program. Only four digital lines are needed to control the 192 CMOS switches, since commands are serial. This allows the system to be easily scaled to larger numbers of microphone elements or additional array chips. The packaged array is connected to the board using a 15 × 15 pin zero insertion force (ZIF) socket for the CPGA package. Batteries are used to provide a ±15 volt analog DC supply and a 4.5 volt digital DC supply.

A detailed circuit diagram of the bias source, sensor, preamplifier, and differential amplifier is shown in Fig. 8. An RC low pass filter is used to reduce the high frequency noise coming from the bias chip. The sensor itself is modeled as a variable capacitor. The current coming from the variable capacitor is fed into a charge amp, constructed from the FET input, low noise operational amplifier AD795 [Analog Devices, Wilmington, MA]. A parallel feedback resistor and capacitor, $C_{fb} = 47 \text{ pF}$ and $R_{fb} = 50 \text{ M}\Omega$, set the low frequency corner of the preamplifier stage at 70 Hz,

TABLE II
ELECTRICAL PROPERTIES OF THE MEMS SENSOR AND SIGNAL CONDITIONING ELECTRONICS

Symbol	Property	Value	Units
C_{sensor}	MEMS sensor capacitance (individual microphone)	~100	pF
R_{filt}	Filter Resistor	10	k Ω
C_{filt}	Filter Capacitor	1	μ F
C_{fb}	Feedback Capacitor	47	pF
R_{fb}	Feedback Resistor	50	M Ω
C_{block}	DC Blocking Capacitor	270	pF
R_{hp}	Resistor to Ground after C_{block}	10	M Ω
f_1	Break Frequency for AD621	200	kHz
G	DC gain of the AD621	100	
k	Boltzmann Constant	$1.38e^{-23}$	J/K

and also set the charge amplifier sensitivity to 21 mV/pC . Since the microphone essentially produces a unit charge for a unit displacement, the value of C_{fb} is indirectly proportional, in a linear sense, to the voltage sensitivity of the system. In addition, it is important that a charge amplifier, rather than a voltage amplifier, be used, so that when additional microphones are switched in by the switch array, the contributions of the microphones will add linearly at the preamplifier output.

After passing through the charge amplifier, the signal passes through a single pole RC high pass filter with a low frequency corner of 60 Hz, and then into a differential amplifier chip [AD621, Analog Devices, Wilmington, MA] which is configured for a voltage gain of 40 dB and a bandwidth of 200 kHz. The AD621 sets the high frequency limit on the system frequency response in the current architecture. In Fig. 8 only one MEMS microphone channel is shown leading to the AD621 noninverting input, but a second identical preamplifier leads to the inverting input, providing three analog outputs for the system : (1) preamplifier output #1 (2) preamplifier output #2 (3) the difference between output (1) and (2).

The noise sources from each component in the electronics have been analyzed to determine the noise floor of the microphone array. Each noise source in Fig. 8 is uncorrelated, and so can be considered separately. Linear circuit theory, using an ideal op-amp model for the AD795, can be applied to determine the transfer functions for each term. The total noise

can be added in a root mean square sense [24]. The various contributions to the total noise, at the AD795 output, are

$$V_{e_{bias}} = \frac{-Z_{fb}C_{sensor}j\omega}{1 + R_{filt}(C_{filt} + C_{sensor})j\omega} e_{bias} \quad (1)$$

$$V_{e_n} = \left(1 + \frac{Z_{fb}C_{sensor}j\omega(1 + R_{filt}C_{filt}j\omega)}{1 + R_{filt}(C_{filt} + C_{sensor})j\omega}\right) e_n \quad (2)$$

$$V_{i_n} = Z_{fb}i_n \quad (3)$$

$$V_{i_{fb}} = Z_{fb}i_{fb} \quad (4)$$

where the feedback impedance is the parallel combination of the feedback components,

$$Z_{fb} = \frac{R_{fb}}{1 + R_{fb}C_{fb}j\omega} \quad (5)$$

The component values are given in Table II. The noise contributions are acted on by the transfer function of the high pass RC filter downstream of the AD795, and a single pole low pass model of the AD621. The resulting noise densities added in an RMS sense, to produce the total noise density estimate at the output of the AD621,

$$V_1 = \left(\sqrt{V_{bias}^2 + V_{e_n}^2 + V_{i_{fb}}^2 + V_{i_n}^2}\right) \frac{C_{block}R_{hp}j\omega}{1 + C_{block}R_{hp}j\omega} \quad (6)$$

$$V_{out} = \left(\sqrt{V_1^2 + e_{inst}^2}\right) \frac{G(2\pi f_1)}{2\pi f_1 + j\omega} \quad (7)$$

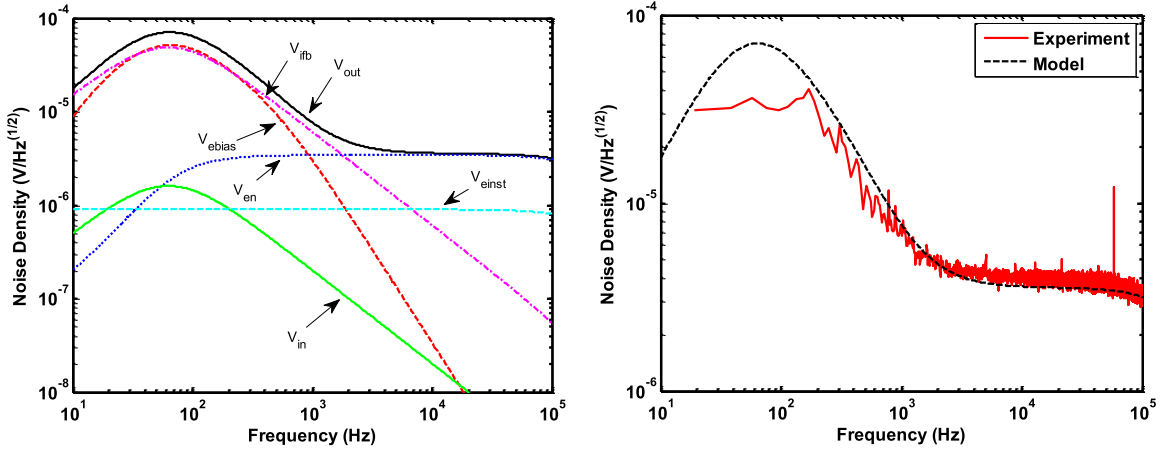


Fig. 9. Electronics spectral noise density. (Left) As computed from a model of the various uncorrelated noise sources in the system. (Right) Model compared to measured noise density.

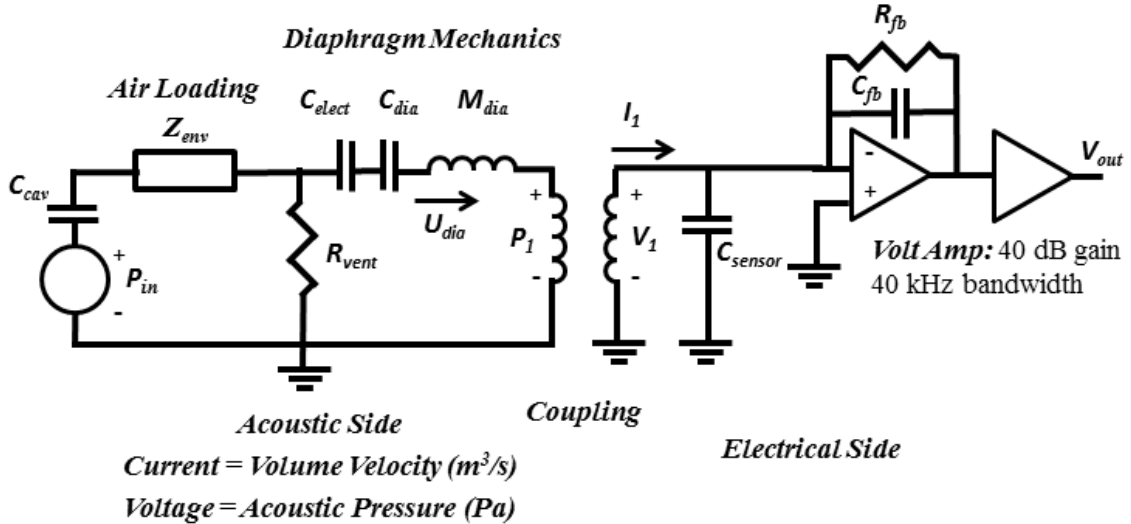


Fig. 10. Coupled electroacoustic lumped element model.

where G is the DC gain of the AD621 amplifier, f_1 is the bandwidth of the AD621, $i_{fb} = \sqrt{4kT/R_{fb}}$, is the Johnson noise from the feedback resistor, $e_{inst} = 9nV/\sqrt{Hz}$ is the instrumentation amplifier voltage noise, $e_n = 11nV/\sqrt{Hz}$, and $i_n = 0.6fA/\sqrt{Hz}$, are the voltage and current noise from the AD795, respectively. The values for e_{inst} , e_n , and i_n come from the data sheets [25], [26]. The bias voltage noise has a corner frequency of 500 Hz, and exhibits a $1/f$ dependence at high frequencies. It is well modeled by

$$e_{bias} = \left(2\mu V/\sqrt{Hz}\right) \frac{2\pi(500Hz)}{2\pi(500Hz) + j\omega} \quad (8)$$

Fig. 9 shows the contribution of each noise source and the RMS total of the noise sources as a whole. As can be seen from Fig. 9, the low frequency noise is dominated by the bias noise and the feedback resistor noise. The feedback resistor then dominates up to the corner frequency of 2 kHz. Above 2 kHz, the noise is dominated by the voltage noise of the AD795. The AD795 current noise and AD621 voltage noise are not major contributions. The model is compared to measured data,

and does an excellent job of predicting system noise. The noise performance for this architecture cannot be significantly improved without major changes to the fabrication process to reduce sensor stray capacitance.

V. MODELING

An electroacoustic lumped element model of the microphone was derived in order to predict an individual microphone sensitivity and frequency response. The deflection of the microphone diaphragm is due to fluctuations in the acoustic pressure adjacent to the diaphragm. This variation in diaphragm deflection changes the capacitance between the diaphragm and bottom electrode, which in turn produces a charge which can be integrated by the charge amplifier to produce a voltage. The model is shown in Fig. 10 as an equivalent circuit.

This model includes various sub-elements: external environmental air loading, diaphragm structural mechanics, electromechanical coupling, backing cavity compliance, air damping, and the negative electrostatic spring. The main

TABLE III
MATERIAL PROPERTIES OF THE LAYERS

Symbol	Property	Value	Units	References
ρ_1	Density of polysilicon	2320	kg/m ³	[38]
ρ_2	Density of Parylene-C	1289	kg/m ³	[39]
E_1	Modulus of Elasticity of polysilicon	158	GPa	[19, 40]
E_2	Modulus of Elasticity of Parylene-C	4.75	GPa	[41]
ν_1	Poisson's Ratio of polysilicon	0.22	-	[19, 40]
ν_2	Poisson's Ratio of Parylene-C	0.4	-	[41]
t_1	Thickness of polysilicon	3.5	μm	Measured
t_2	Thickness of Parylene-C	2	μm	Measured

result of interest from the model is the volume velocity of the diaphragm, U_{dia} , which can be related to the observed diaphragm motion, and the voltage output of the electronics, V_{out} , which is the measured microphone signal. The modeling procedure closely follows the methods described in Doody *et. al* [27]. The most significant difference from Doody's model is that this device has holes through the diaphragm to front vent the device.

Mechanically, the diaphragm is modeled as an elastic, isotropic circular plate with uniform pressure loading and clamped boundary conditions. The deflection at low frequencies is [28]

$$u(r) = \frac{pa^4}{64D} \left(1 - \left(\frac{r}{a}\right)^2\right)^2 \quad (9)$$

where r is the radial position, p is the applied pressure, $a = 0.3 \text{ mm}$ is the diaphragm radius, and D is the bending stiffness for a classical thin laminate plate, which can be derived from the description in Budynas [29],

$$D = \sum_n \frac{E_n}{1 - \nu_n^2} \left(\frac{t_n^3}{12} + t_n y_n^2\right) \quad (10)$$

where E_n , ν_n and t_n are the elastic modulus, Poisson ratio, and thickness of the n^{th} layer. Material properties for the layers are given in Table III. y_n is the distance from the center of the n^{th} layer to the neutral axis, which can be computed from

$$y_c = \frac{\sum_n z_n \left(\frac{E_n t_n}{1 - \nu_n^2}\right)}{\sum_n \frac{E_n t_n}{1 - \nu_n^2}} \quad (11)$$

$$y_n = z_n - y_c \quad (12)$$

where y_c is the position of the neutral axis with respect to the bottom of the laminate and z_n is the position of the center of the n^{th} layer with respect to the bottom of the laminate.

The electrostatic model for the diaphragm and backing electrode acting as a parallel plate capacitor is taken from the work of Doody *et. al* [27]. The electrostatic force per unit area is an effective pressure,

$$P_{eff} = \frac{\frac{1}{2} V^2 \epsilon_0}{(g_0 - \Delta g)^2} \quad (13)$$

where V is the applied voltage, ϵ_0 is the permittivity of free space, g_0 is the initial gap, and Δg is the gap change. The gap change is non-uniform and follows the displacement, $u(r)$, hence

$$P_{eff}(r) = \frac{\frac{1}{2} V^2 \epsilon_0}{(g_0 - u(r))^2} \quad (14)$$

where, by using the static deflection shape, $u(r)$, the implicit assumption is that deflections are occurring at frequencies where the static modeshape is dominant. This will be a reasonable model at frequencies below the first resonant frequency of the structure. During operation, the microphone is held at a constant bias voltage, V_{bias} . By integrating the effective electrostatic pressure over the diaphragm, and collecting terms that are first order in $u(r)$, we arrive at the electrostatic coupling coefficient, N , and the compliance of the negative electrostatic spring, C_{elect} , assuming small deflections. The derivation is given in [27]

$$N = \frac{V_{bias} \epsilon_0}{g_0^2} \quad (15)$$

$$C_{elect} = \frac{-g_0^3}{V_{bias}^2 \epsilon_0} \quad (16)$$

where the electromechanical coupling between pressure and voltage, as shown in the diagram, is

$$P_1 = N \cdot V_1 \quad (17)$$

$$I_1 = N \cdot U_{dia} \quad (18)$$

The environmental mass loading, Z_{env} , represents the acoustic radiation impedance of the circular vibrating diaphragm radiating into an infinite half-space. The model of environmental loading is taken directly from the work of Porter [30]. This model is for a circular diaphragm in an infinite planar baffle oscillating in the static clamped modeshape of equation (9), transmitting into an infinite acoustic halfspace. The model is valid up to very high values of ka , where $k = \omega/c$ is the acoustic wavenumber and a is the diaphragm radius. Expressed as an acoustic element, the environmental self-impedance for the diaphragm from equation 18 of Porter is

$$Z_{env} = \frac{18\rho c}{\pi a^2} \sum_{k=0,2,4} \sum_{l=0,2,4} \alpha_k \alpha_l (S_{kl} + jT_{kl}) \quad (19)$$

where the properties of air are taken to be $\rho = 1.21 \text{ kg/m}^3$, $c = 343 \text{ m/s}$. From the reference, for the clamped circular diaphragm, $\alpha_0 = 1$, $\alpha_2 = 2$, $\alpha_3 = 1$. The expressions for S_{kl} and T_{kl} are lengthy and need not be reproduced here; they are given in terms of Bessel and Struve functions in Tables I and II of Porter [30]. It is noted that Porter also provides expressions for the mutual radiation impedance between multiple oscillating elements. These mutual radiation impedances can be used to include acoustic coupling between elements in the array, resulting in a fully coupled array model, in a manner similar to that one in [42]. Such an array model was created and implemented. For the current array, the effects of mutual radiation impedance on the dynamics were found to be negligible. However, it is noted that if a similar array were operated in a heavier fluid, such as water, mutual radiation impedance could play an important role in the dynamics and should be considered.

The standard compliance of a rigid air filled cavity [27], [31] is used

$$C_{cav} = \frac{V_{gap}}{\rho c^2} \quad (20)$$

where $V_{gap} = \pi a^2 g_0$ is the volume of the gap between the diaphragm and bottom electrode. From Martin *et al.*, we take the compliance of the diaphragm (for a two layer thin laminate clamped circular bending plate), and the effective mass of the diaphragm (for the first mode of the same two layer thin laminate clamped circular bending plate) [32],

$$C_{dia} = \frac{\pi a^6}{192 D} \quad (21)$$

$$M_{dia} = \frac{9(\rho_1 t_1 + \rho_2 t_2)}{5\pi a^2} \quad (22)$$

where, t_1 is the thickness of the polysilicon, t_2 is the thickness of Parylene-C, ρ_1 is the density of polysilicon, ρ_2 is the density of Parylene-C, a is the radius of the diaphragm, and D is the effective bending stiffness of the laminate plate, which was defined previously.

Finally, we must estimate the viscous damping due to flow through the holes and in the cavity. We use Škvor's formula [33] to estimate the resistance due to squeeze film damping, R_{sq} , in between the perforated diaphragm and the backing electrode,

$$R_{sq} = \frac{12\mu C_f}{n\pi g_0^3} \quad (23)$$

where $\mu = 1.9 \cdot 10^{-5} \text{ Pa}\cdot\text{s}$ is the viscosity of air, $n = 28$ is the number of holes in the diaphragm, and the expression C_f from [33] is computed from the area fraction of holes to the total plate as

$$S = \frac{na_{hole}^2}{a^2} \quad (24)$$

$$C_f = \frac{S}{2} - \frac{3}{8} - \frac{S^2}{8} - \frac{1}{4} \ln(S) \quad (25)$$

$a_{hole} \approx 1 \text{ }\mu\text{m}$ is the radius of the holes in the diaphragm. The viscous resistance due to flow through small holes in a perforated diaphragm is [34]

$$R_{hole} = \frac{8\mu (t_1 + t_2 + \frac{3}{8}\pi a_{hole})}{n\pi a_{hole}^4} \quad (26)$$

where the hole radius, for in air operation, should be $a_{hole} < 0.002/f^{1/2}$, f in Hz , a_{hole} in meters, according to Beranek [28]. At a resonant peak frequency of 440 kHz, where damping is most important, this result should be used for holes with a radius $a_{hole} < 3 \text{ }\mu\text{m}$, valid for the device presented here. The total vent hole resistance is the series combination of the two components,

$$R_{vent} = R_{hole} + R_{sq} \quad (27)$$

Note that this resistive element is in parallel with the cavity compliance, and thus neglects additional squeeze damping that would be present due to air motion from compression in the backing cavity (which would be in series with the cavity compliance). It is assumed that the damping from flow to and through the diaphragm holes is dominant over flow due to nonuniform compression in the gap. Other damping models are also possible for a perforated diaphragm such as this. For example, the work of Homentcovshi and Miles [34] explores the damping and mass loading of a perforated diaphragm at MEMS scales, including the effects of compressibility, fluid inertia, and slip boundary conditions at low Knudsen numbers. The damping derivation is given fully in the reference, but reduces to Škvor's formula if these effects are neglected and viscous losses for incompressible flow in the gap with non-slip boundary conditions dominate. The full model from Homentcovshi and Miles was applied to the case being considered here and gave nearly identical results to Škvor's formula, indicating that the simpler model of Škvor is sufficient for this case.

Using this model, the sensitivity and frequency response of an individual microphone in the array can be computed. All material properties for the calculation are given in Table III. The final predicted pressure sensitivity results are shown in Fig. 11 for two different vent hole sizes. This is the

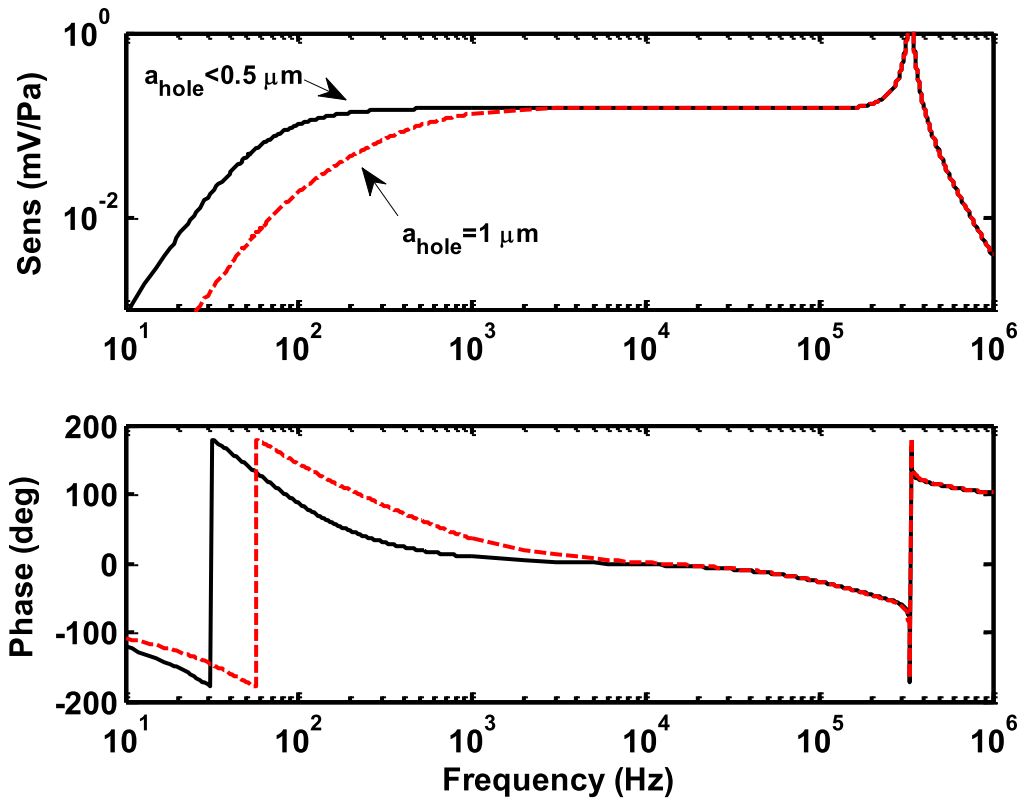


Fig. 11. Predicted acoustic sensitivity for a single element including electromechanical model and amplifier models. Results are shown for small vent holes ($a_{\text{hole}} < 0.5 \mu\text{m}$) and $1 \mu\text{m}$ radius vent holes.

sensitivity at the instrumentation amplifier (AD621) output, and includes the AD621 gain of 100 and single pole amplifier model, as well as the ideal opamp model of the AD795 preamp and the various linear circuit elements as detailed in the circuit diagrams. In all cases, a DC bias of 10 V is used.

In the midband, the predicted sensitivity of a single element is 0.15 mV/Pa . The first air loaded resonant frequency of the diaphragm is at 340 kHz and exhibits very little damping. The -3 dB point occurs at 430 kHz . This bandwidth is set by the gain bandwidth product of the AD621 and the mechanical resonance of the diaphragm. Varying the size of the vent holes sets the predicted low frequency bandwidth. With vent holes sized at $0.5 \mu\text{m}$ radius or smaller, the low frequency bandwidth extends to 100 Hz , where it is set by the feedback components in the preamp. With $1 \mu\text{m}$ radius vent holes, the low frequency -3 dB point is at 625 Hz . Hence, during Parylene coating, the target is to reduce the effective vent hole size to approximately $0.5 \mu\text{m}$ radius, without completely sealing the holes, which would cause diaphragm collapse due to static pressure differences.

VI. CHARACTERIZATION

The electronics were characterized first to ensure that sufficient isolation was achieved between the various microphone channels. Fig. 12 shows that the on/off isolation and crosstalk measurements. The tests are conducted by substituting a dummy capacitor of size 47 pF for the MEMS sensor, driving with an oscillating voltage (which produces an oscillating

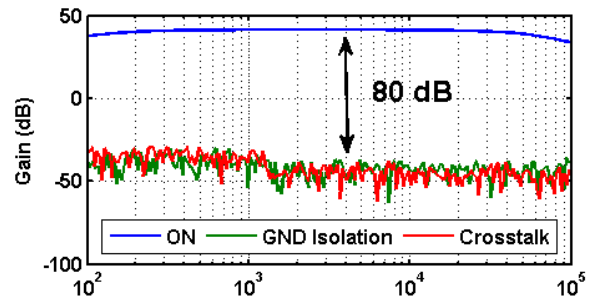


Fig. 12. Isolation measurements taken by driving a channel through a dummy capacitor, and measuring the system output when the channel was switched on or switched to ground. Crosstalk was measured by driving one channel which was switched to ground, and measuring on an adjacent channel that was switched on.

charge), and measuring the system output. When the driven channel is switched on via the CMOS switch, the voltage gain is 40 dB re 1 V/V . When the channel is grounded, the gain drops to below -40 dB . If a channel adjacent to the driven channel is switched on, then the gain remains below -40 dB re 1 V/V . Both scenarios result in an approximately 80 dB reduction in signal, indicating good performance in terms of off isolation and cross talk.

A laser Doppler vibrometry system [Polytec OFV 511 fiber interferometer] was used to measure the diaphragm mechanical response to an electrostatic excitation. The out of plane displacement of the membrane was measured when an oscillating voltage consisting of a 9 V_{DC} bias and a

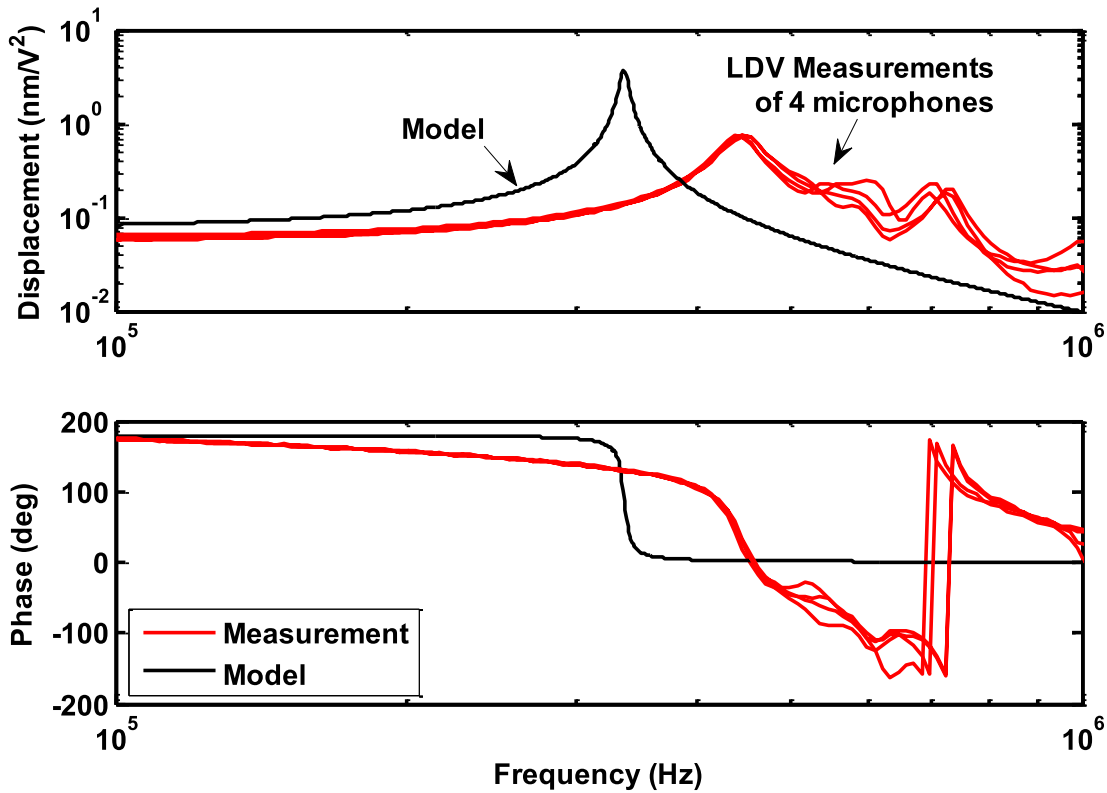


Fig. 13. Laser Doppler vibrometry data showing the electrostatically driven frequency response of five microphones off of one chip compared to two models.

1 V_{peak} drive was applied. The theoretical model of Fig. 10 can be applied to this case by setting the external acoustic pressure, P_{in} , to zero, and applying a voltage to the ideal transformer, $V_1 = (1V)e^{j\omega t}$. The DC bias is now 9V. The response of five different microphones in the array is shown in Fig. 13 compared to the theoretical model. The displacement amplitude is normalized by the product of the applied AC and DC voltages, as is appropriate considering the square law nature of the electrostatic force.

The four microphones shown are well matched to each other in terms of absolute amplitude, phase, and resonant frequency. Some deviation is seen above the first resonance, but this is outside the operation range of the sensor. The measured resonant frequency of the microphones is 440 kHz, and the low frequency displacement amplitude is 0.06 nm/V^2 . The model does a reasonable job of predicting the absolute displacement and the first resonant frequency of the microphone. The model predicts a first resonance frequency of 340 kHz and a low frequency displacement of 0.09 nm/V^2 . One possible explanation for the difference is that tensile residual stresses are present in the diaphragm. The residual stresses in the polyMUMPS polysilicon layers, as measured by MEMSCAP for PolyMUMPS Run 86, were less than 5 MPa, and were slightly compressive. Hence, if significant tensile stresses are indeed present, these stresses must be introduced during epoxy curing or other packaging steps. This is possible, but seems unlikely, particularly given the good agreement to the model at low frequencies as seen in Fig. 16.

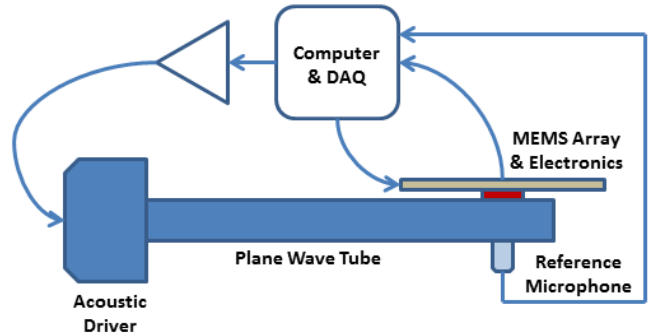


Fig. 14. Plane wave tube acoustic calibration setup.

An alternative explanation for the discrepancies between the model and the data is that the structural and acoustic approximations made in the lumped element model are introducing errors at high frequencies. This seems likely, as at 440 kHz, the wavelength of sound in air is 0.78 mm, only slightly larger than the microphone diameter. Additional evidence supporting this explanation is the excellent match obtained between acoustic calibration data and the model, with no residual stresses, as seen in Fig. 16. In any case, the model is predictive at frequencies below 100 kHz, which are of primary interest for the testing described below.

Acoustic calibration of the microphones in the array was carried out using a plane wave tube, as shown in Fig. 14. The MEMS array was flush mounted on one side of the tube, across from a Brüel and Kjær Type 4939 $\frac{1}{4}$ "

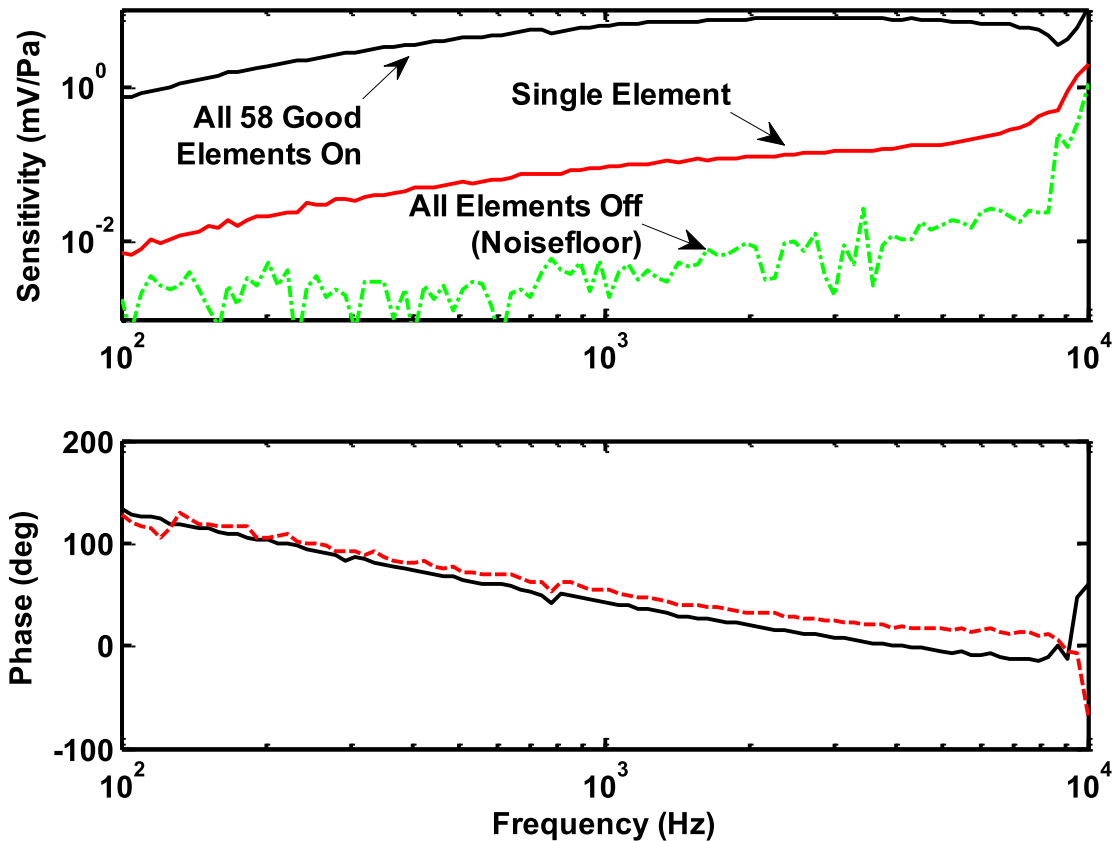


Fig. 15. Plane wave tube calibration of the MEMS array compared to a B&K 4939 microphone. Curves are shown for all 58 good elements turned on (acting in parallel), a single element on, and all elements off.

condenser microphone. An acoustic driver was used to generate plane waves in the tube. The tube is 12.7 mm \times 12.7 mm in cross-section, and rigidly terminated at a location approximately 1 cm from the center of the chip. Standing waves build up in the tube, allowing testing at high sound pressure levels. The system is limited to calibrations below 13 kHz. Above 13 kHz higher order modes cut on and the reference microphone will no longer see the same acoustic pressure as the MEMS device. In addition, due to the rigid termination, the first pressure null will pass the test location at a frequency between 5 kHz and 10 kHz, resulting in a peak in the calibration curve which should be discarded. The entire system is housed in a double Faraday cage, with a second cage around the acoustic driver, in order to reduce electromagnetic interference. The driver is controlled in a closed loop fashion during the frequency sweep to hold the delivered sound pressure level constant at 130 dB SPL across all frequencies tested.

A typical frequency response is shown in Fig. 15, where three curves are presented. The highest sensitivity curve is for all good microphones on this chip turned on, so they all contribute charge in parallel. It is emphasized that in this configuration, all 58 good microphone outputs are summing in parallel at the charge preamplifier. The middle curve is for a single microphone on, and all other microphones off. The bottom curve is for all microphones turned off, and represents the noise floor for the measurement which

includes electromagnetic interference, random noise sources, and room acoustic contamination. In the mid band at 1 kHz, the single microphone sensitivity is 0.1 mV/Pa. For 58 microphones in parallel, the sensitivity at 1 kHz is 6.2 mV/Pa, suggesting an average sensitivity of 0.11 mV/Pa for the 58 microphones. The -3 dB bandwidth, as measured using the 58 microphone group, is from 700 Hz to greater than 10 kHz, although after taking into account the measured calibration curve, the microphones can be used to measure turbulent pressures below 700 Hz. Calibration is limited 10 kHz for reasons previously explained, however LDV results suggest that the microphone could be used at frequencies up to 440 kHz (first resonance), if the electronics were able to support the larger bandwidth. Currently the high frequency limit of 200 kHz is set by the bandwidth of the differential amplifier chip. The phase is smooth and well matched between the two cases. The rise in the frequency response of the individual microphone observed above 5 kHz is due to the first pressure null passing the reference microphone location and is an artifact of the calibration scheme, not a feature of the microphone response. Measurements of this type were conducted for all 58 good microphone elements on the chip. As shown in Fig. 16, 51 of the 58 working microphones exhibit sensitivities with deviations in magnitude and phase at 1 kHz of ± 2.5 dB and ± 6.5 degrees. When the chip was initially calibrated, all 59 working microphones fell within this range, but after storage and operation in various testing environments

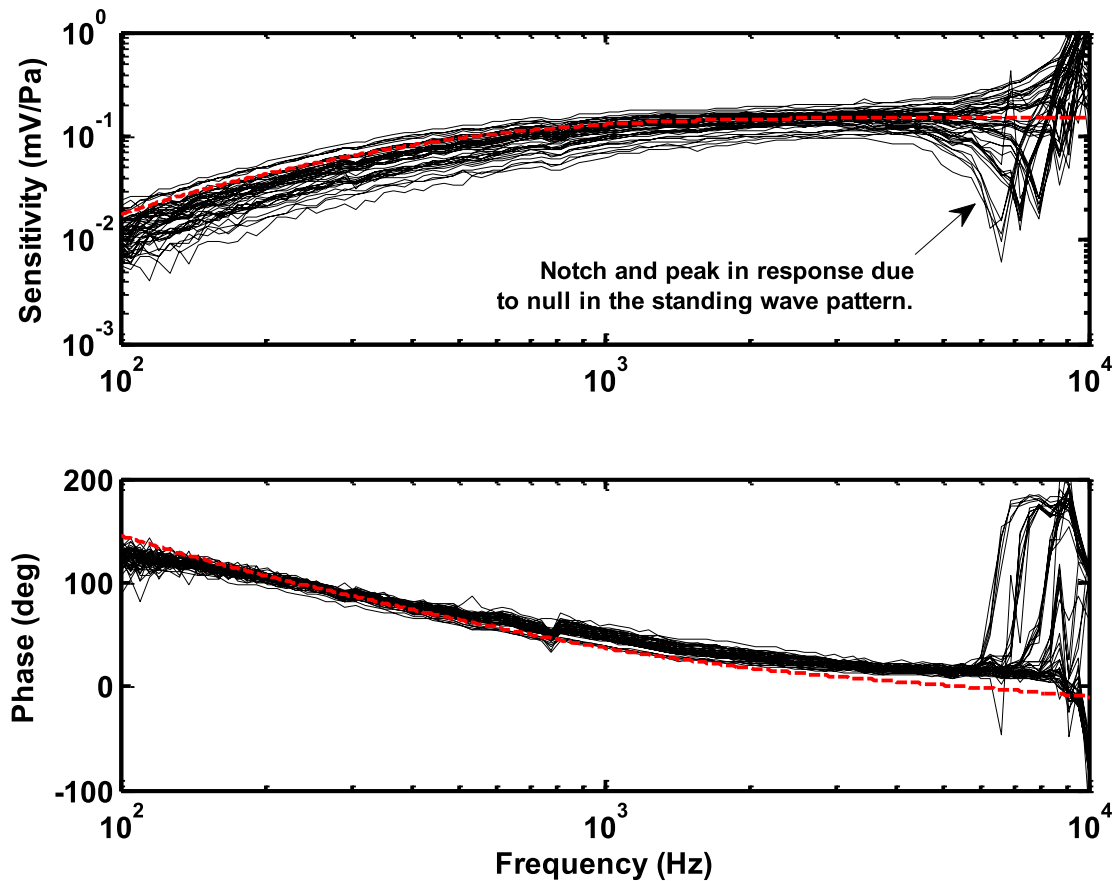


Fig. 16. Plane wave tube calibration result for each of the 51 most closely matched individual elements (thin black lines), compared to the computational model (heavy dashed red line). The best fit was achieved using zero residual stress and a vent hole radius of $1 \mu\text{m}$.

over the course of 2 years, including windtunnel testing at Mach 0.6, and multiple cross-country trips, 1 microphone failed and 7 microphones showed larger than 2.5 dB sensitivity deviation. The individual calibration curves are repeated before any given test and used to compensate for the differences between the individual elements in post processing.

The measured frequency responses of the 51 best microphones are also compared to the computational predictions from the model in Fig. 16. To achieve the best match between the measured and modeled results, the vent hole radius was set to $1 \mu\text{m}$. As fabricated, the vent holes have a radius of approximately $3\text{-}4 \mu\text{m}$, and $2 \mu\text{m}$ of Parylene was deposited, so this is very reasonable. Additional low frequency bandwidth could be recovered on this chip by depositing an additional $0.5 \mu\text{m}$ of Parylene.

Single frequency calibrations were carried out at 1 kHz to determine the linearity of the MEMS microphone response at high sound pressure levels. The result is shown in Fig. 17. The data is for a single microphone in the array, and demonstrates better than 0.3% nonlinearity at 150 dB SPL.

The noise density of the output with the MEMS array turned on, but no acoustics present, was also measured in order to determine the microphone resolution. The results are shown in Fig. 18. The result is given after dividing by the sensitivity and converting into dB SPL (re $20 \mu\text{Pa}$) in a 1 Hz band. The sensitivity used in the conversion was for a single

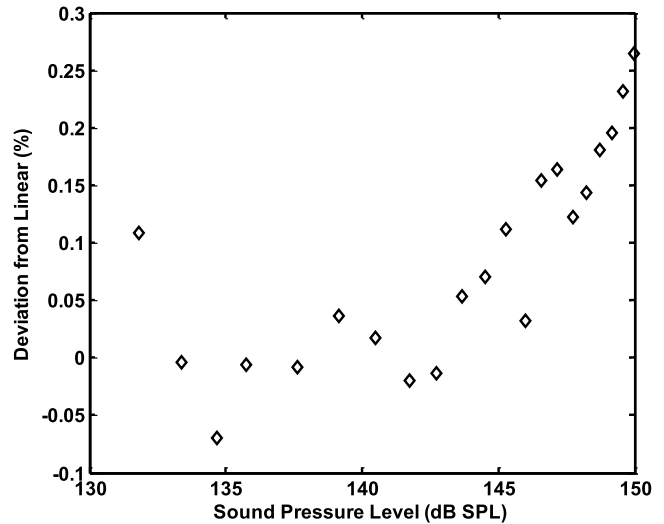


Fig. 17. Deviation of output from linear for a single element at 1 kHz and 10 V bias.

microphone in the array. Thus, the resulting noise density for 58 elements in parallel would be 58 times (35 dB) lower. In the mid band from 1 kHz to 10 kHz, the resolution of a single microphone is 63 dB SPL in a 1 Hz band. For the entire chip acting in parallel, the resolution is 28 dB SPL in a 1 Hz band.

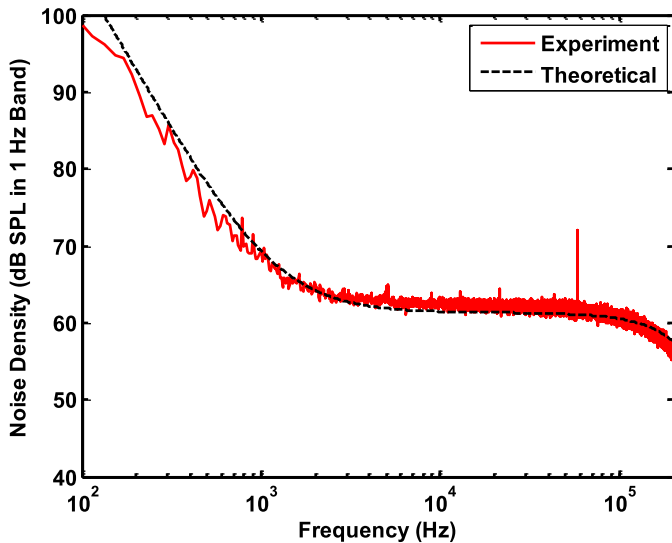


Fig. 18. Noise density plot showing measured noise density compared to model predictions. The results are presented after dividing by the sensitivity of a single microphone and converting into dB SPL (re $20 \mu\text{Pa}$) in a 1 Hz band.

VII. WIND TUNNEL TESTING

The microphone array in the CPGA package was flushed mounted into a precision machined square cutout in an aluminum plate, the sides were sealed with modeling clay and smoothed flat with a razor blade, and then the plate was mounted into the side of a $150 \text{ mm} \times 150 \text{ mm}$ square duct flow facility at Spirit Aerosystems in Wichita, KS. The flow duct is supplied by three lines of house compressed air merged together for a smooth transition by a 3 to 1 mixer. The air flow travels down an a Universal silencer (model number U2C-10) and into a diffuser assembly where a series of screens create a laminar flow to enter a settling chamber. The settling chamber has damping tiles attached to the outside to reduce noise and structural vibrations during operation. The inlet assembly leads to a nozzle that transitions the round cross section to the square cross section of the test section. Care was taken to design a nozzle with a smooth transition from the round to square cross section without generating additional turbulence. The flow duct itself is 7 meters long with a 1 meter long test section. The sensor array was mounted 3.239 m from the exit of the contraction assembly, as shown in Fig. 19. At the full $150 \text{ mm} \times 150 \text{ mm}$ cross section, the tunnel can currently run up to Mach 0.6. Additional details on the flow facility, including acoustic characterization data, can be found in [35] and [36].

Structural vibrations can be a significant source of error in wind tunnel measurements. In order to mitigate this effect, vibration isolation mounts consisting of compressed rubber grommets were employed in an attempt to decouple the test electronics from structural vibrations. In addition, two accelerometers were recorded during tunnel measurement to capture structural vibrations on the tunnel wall and on the MEMS test electronics. The coherence between the accelerometer signal and the MEMS sensor measurements can be used to identify any regions of the spectrum where structural vibrations are causing contamination of the measurement.

During the test, the signals coming from four Kulite MIC-093 high intensity pressure sensors and a Brüel & Kjær type 4136 $\frac{1}{4}$ inch pressure microphone were also recorded. The Kulite sensors were placed within 20 cm of the MEMS array, as shown in Fig. 19. They were recess mounted in 0.8 mm diameter, 1.4 mm long pinholes, which create a Helmholtz resonance at approximately 10 kHz. The B&K microphone was flush mounted on the opposite side of the flow duct with the screen removed.

Measurements were made at six flow rates from Mach 0.1 to Mach 0.6. The eight channels (two MEMS channels, B&K, 4 Kulites, one accelerometer) were sampled in each of thirty eight different array configurations at 120 kS/s for 1 second. From these different configurations it will be possible to extract information about the wavenumber content of the pressure fluctuations in addition to their frequency content. The purpose of this paper is not to completely analyze the data set; rather, in this work we are focused on describing the measurement system and demonstrating its capabilities.

To that end, a power spectral density plot is presented in Fig. 20. The plot compares the power spectral density measured by the MEMS array, one of the Kulite sensors, and the B&K 4136. In all three cases, the data was processed using an 8192 sample, 50% overlap Hanning window to produce averaged power spectra in V^2/Hz . The calibration curves measured in the plane wave tube were applied to the MEMS data to put it into engineering units of Pa^2/Hz . The B&K and Kulite were calibrated at a single frequency using an acoustic calibrator prior to testing. For this data, the MEMS array was configured with the four central sensors in the array turned on, and the remaining sensors turned off. Thus, the array is measuring the single point wall pressure spectrum with an aperture of approximately 2 mm. As can be seen from the figure, excellent agreement between the measured pressure spectrum is achieved between the MEMS sensor array, the Kulite, and the B&K at frequencies from 300 Hz to 3 kHz. Between 3 kHz and 10 kHz, the Kulite deviates from the other two sensors. This deviation is attributed to the Helmholtz resonance of the Kulite mounting pinhole. The MEMS array and B&K agree up to 10 kHz, where the B&K begins to deviate from the MEMS array. Above 10 kHz, spatial averaging effects may be more important. These effects have been explored (e.g. [6] and [37]) and will be described elsewhere, but are outside the scope of the present work.

Structural vibration sensitivity is seen at frequencies between 100 and 300 Hz. This is known to be structural vibration due to high coherence with the accelerometer data. The MEMS system appears to have higher structural vibration sensitivity than the other two sensors. This is attributed to the electronics. Since the MEMS system electronics are surface mounted on a relatively large printed circuit board, structural vibration can cause flexing of the board and generate signals in the high gain electronics. Structural vibration sensitivities are associated with the preamplifier channels, not with the MEMS elements; if the MEMS sensors are switched off using the CMOS switch array, structural sensitivity remains. Regardless, this is not a major concern since the majority of the structural vibrations are at low frequencies, below the main frequencies

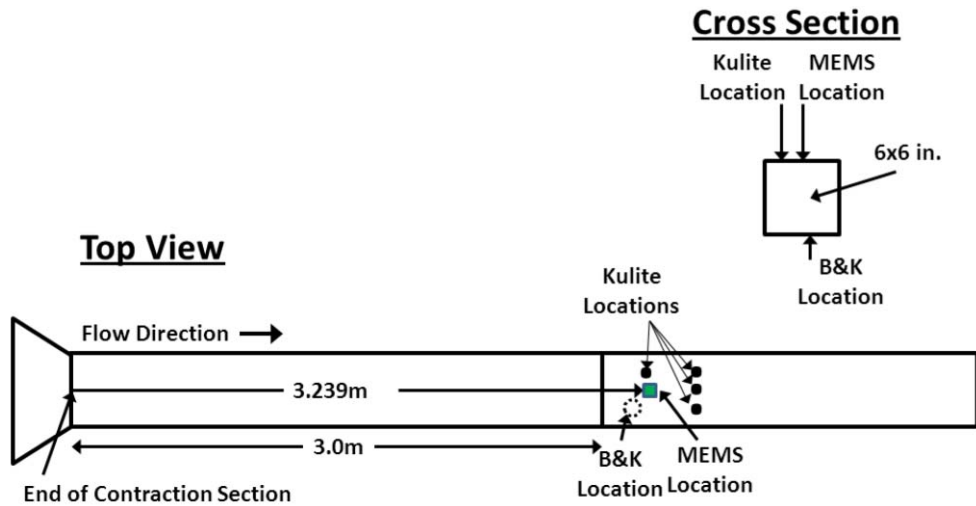


Fig. 19. Wind tunnel experiments were carried out from Mach 0.1 to Mach 0.6 with the MEMS array flush mounted in the wall of the 15 cm × 15 cm square test section, 3.24 m from the end of the contraction section. Four Kulite transducers and a B&K microphone were also used during the tests.

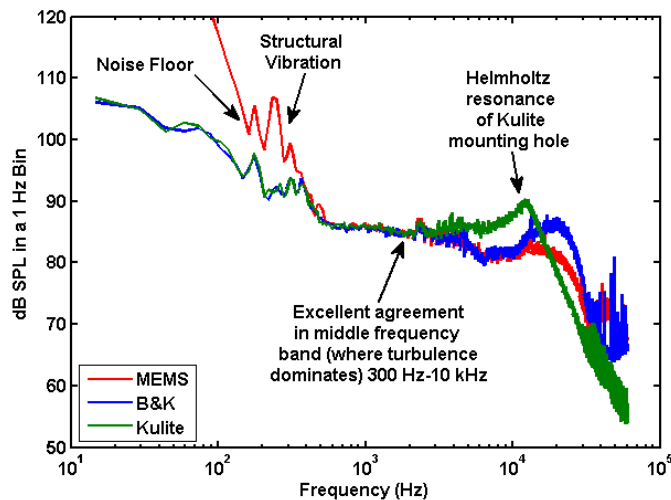


Fig. 20. In wind tunnel testing at Mach 0.3, the MEMS array power spectra is compared to two commercial pressure transducers showing excellent agreement in the 300 Hz to 10 kHz bandwidth. The MEMS array is configured with the 4 central elements turned on.

of interest for turbulence (1-10 kHz). Similar results were obtained at all flow rates where the turbulent and acoustic pressures in the duct exceed the noise floor by 3 dB or more (Mach 0.3 and above).

After exposure to the flow environment at Mach numbers up to 0.6, the MEMS array was tested to see if any elements had large static capacitance or resistance changes that would be indicative of element failure. In addition, all elements were recalibrated in the plane wave tube. No elements failed during flow testing at the Spirit Aerosystems facility, nor were any microphones damaged while testing in a Mach 0.5 14” inflow wind tunnel at NASA Ames Research Center at a later date. One microphone ceased functioning for unknown reasons during transport or storage of the array in the approximately 2 year gap between the Spirit Aerosystems test and the NASA Ames test. Overall, the robustness of the system appears sufficient for testing in laboratory wind tunnels. Testing in

flight presents additional challenges due to the presence of moisture and particulates. Flight testing has not yet been attempted. The Parylene C coating is expected to give some level of protection to the system (the entire surface including all interconnects is coated in Parylene) but additional testing is required to examine robustness and environmental issues.

VIII. CONCLUSION

A novel architecture for a MEMS microphone array on a chip and associated system level electronics has been introduced. The system is targeted at measurement of the pressure fluctuations beneath the turbulent boundary layer with high spatial resolution. The individual elements have a diameter of 0.6 mm. Sixty four elements are arrayed on a square die with a center to center spacing on the order of 1.25 mm, can operate from approximately 100 Hz to 200 kHz, and exhibit less than 0.3% nonlinearity at 150 dB SPL. A packaging methodology was developed to keep surface topology below 0.13 mm. Modeling and calibration have been carried out successfully to understand the dynamics and noise sources.

The system was tested in a high speed flow duct at speeds up to Mach 0.6. Excellent agreement was seen between the MEMS array and two commercial transducers at mid band frequencies. The MEMS array has higher spatial resolution and bandwidth. The system has applications not only in turbulence measurement, but in all types of unsteady flows, such as turbomachinery wakes and wakes from biological specimens, that may contain significant flow features in the 100 Hz–100 kHz band at scales less than 1 cm. Future work will focus first on first fully analyzing the flow duct experimental data to produce estimates of wavenumber frequency spectra, and then move on to improving board level packaging to reduce vibration sensitivity, creating larger arrays using multiple co-packaged chips, and running additional transient flow experiments for other applications. In addition, efforts will be made to reduce frontside surface topology by moving to through silicon vias and backside contacts.

REFERENCES

- [1] B. M. Abraham and W. L. Keith, "Direct measurements of turbulent boundary layer wall pressure wavenumber-frequency spectra," *J. Fluids Eng.*, vol. 120, no. 1, pp. 29–39, 1998.
- [2] W. V. Bhat, "Flight test measurement of exterior turbulent boundary layer pressure fluctuations on Boeing model 737 airplane," *J. Sound Vibrat.*, vol. 14, no. 4, pp. 439–457, 1971.
- [3] W. K. Blake and D. M. Chase, "Wavenumber-frequency spectra of turbulent-boundary-layer pressure measured by microphone arrays," *J. Acoust. Soc. Amer.*, vol. 49, no. 3B, pp. 862–77, 1971.
- [4] M. K. Bull, "Wall-pressure fluctuations beneath turbulent boundary layers: Some reflections on forty years of research," *J. Sound Vibrat.*, vol. 190, no. 3, pp. 299–315, 1996.
- [5] W. M. Humphreys, Jr., T. F. Brooks, W. W. Hunter, Jr., and K. R. Meadows, "Design and use of microphone directional arrays for aeroacoustic measurements," in *Proc. 36th Aerosp. Sci. Meet. Exhibit*, Reno, NV, USA, 1998, pp. 98–471.
- [6] R. M. Lueptow, "Transducer resolution and the turbulent wall pressure spectrum," *J. Acoust. Soc. Amer.*, vol. 97, no. 1, pp. 370–378, 1995.
- [7] E. Kalvesten, "Pressure and wall shear stress sensors for turbulence measurements," Ph.D. dissertation, Dept. Signals Sens. Syst., Royal Inst. Technol., Stockholm, Sweden, 1996.
- [8] T. M. Farabee and F. E. Geib, "Measurement of boundary layer pressure fields with an array of pressure transducers in a subsonic flow," in *Proc. ICASF*, 1975, pp. 311–319.
- [9] D. P. Arnold, T. Nishida, L. N. Cattafesta, and M. Sheplak, "A directional acoustic array using silicon micromachined piezoresistive microphones," *J. Acoust. Soc. Amer.*, vol. 113, no. 1, pp. 289–298, 2003.
- [10] A. Berns, U. Buder, E. Obermeier, A. Wolter, and A. Leder, "AeroMEMS sensor array for high-resolution wall pressure measurements," *Sens. Actuators A, Phys.*, vol. 132, no. 1, pp. 104–111, 2006.
- [11] J. Krause, R. White, M. Moeller, J. Gallman, and R. De Jong, "MEMS pressure sensor array for aeroacoustics analysis of the turbulent boundary layer," in *Proc. AIAA Infotech*, Seattle, WA, USA, 2009, pp. 1–4.
- [12] J. Krause, R. White, M. Moeller, J. Gallman, and R. De Jong, "MEMS pressure sensor arrays for aeroacoustics analysis of the turbulent boundary layer," in *Proc. ASME Int. Mech. Eng. Congr. Exposit.*, Boston, MA, USA, 2008, pp. 1–4.
- [13] R. D. White, J. Krause, R. De Jong, G. Holup, J. Gallman, and M. Moeller, "MEMS microphone array on a chip for turbulent boundary layer measurements," in *Proc. AIAA Aerosp. Sci. Meet.*, Nashville, TN, USA, 2012, pp. 1–8.
- [14] R. D. White, J. Krause, S. Liu, Z. Zhao, J. Gallman, and M. Moeller, "Array-on-a-chip pressure and shear stress sensors for boundary layer characterization," in *AIAA Aerosp. Sci. Meet.*, Orlando, FL, USA, Jan. 2011.
- [15] M. Goody, "Empirical spectral model of surface pressure fluctuations," *AIAA J.*, vol. 42, no. 9, pp. 1788–1794, 2004.
- [16] J. S. Krause, "Micromachined microphone array on a chip for turbulent boundary layer measurements," Ph.D. dissertation, Dept. Mech. Eng., Tufts Univ., Medford, MA, USA, 2011.
- [17] L. Lofdahl and M. Gad-el-Hak, "MEMS-based pressure and shear stress sensors for turbulent flows," *Meas. Sci. Technol.*, vol. 10, no. 8, pp. 665–686, 1999.
- [18] H. Tennekes and J. L. Lumley, *A First Course in Turbulence*. Cambridge, MA, USA: MIT Press, 1972.
- [19] J. Carter, A. Cowen, B. Hardy, R. Mahadevan, M. Stonefield, and S. Wilcenski, *PolyMUMPs Design Handbook*, Rev. 11, Durham, NC, USA: MEMSCAP, Inc., 2005.
- [20] D. C. Miller, B. L. Boyce, M. T. Dugger, T. E. Buchheit, and K. Gall, "Characteristics of a commercially available silicon-on-insulator MEMS material," *Sens. Actuators A, Phys.*, vol. 138, no. 1, pp. 130–144, 2007.
- [21] R. W. Johnstone and M. Parameswaran. (2002). *MUMPs Design Handbook: Unofficial Supplement* [Online]. Available: <http://www.sfu.ca/immr/>
- [22] J. Chen, L. Liu, Z. Li, Z. Tan, Y. Xu, and J. Ma, "Single-chip condenser miniature microphone with a high sensitive circular corrugated diaphragm," in *Proc. IEEE Micro Electro Mech. Syst.*, Jan. 2002, pp. 284–287.
- [23] D. C. Miller, W. L. Hughes, Z.-L. Wang, K. Gall, and C. R. Stoldt, "Mechanical effects of galvanic corrosion on structural polysilicon," *J. Microelectromech. Syst.*, vol. 16, no. 1, pp. 87–101, Feb. 2007.
- [24] S. Iep, "Low-noise preamplifier for capacitive sensors," M.S. thesis, Dept. Electr. Eng. Comput. Sci., Massachusetts Inst. Technology, Cambridge, MA, USA, 1995.
- [25] Analog Devices, "Low drift, low power instrumentation amplifier," *AD621 Datasheet Rev. B*, pp. 1–16, 2001.
- [26] Analog Devices, "Low power, low noise precision FET op amp," *AD795 Datasheet Rev. C*, pp. 1–20, 2009.
- [27] C. B. Doody, X. Cheng, C. A. Rich, D. F. Lemmerhirt, and R. D. White, "Modeling and characterization of CMOS-fabricated capacitive micro-machined ultrasound transducers," *J. Microelectromech. Syst.*, vol. 20, no. 1, pp. 104–118, Feb. 2011.
- [28] J. N. Reddy, *Theory and Analysis of Elastic Plates and Shells*, 2nd ed. Boca Raton, FL, USA: CRC Press, 2007.
- [29] R. G. Budynas, *Advanced Strength and Applied Stress Analysis*, 2nd ed. New York, NY, USA: McGraw-Hill, 1999.
- [30] D. T. Porter, "Self- and mutual-radiation impedance and beam patterns for flexural disks in a rigid plan," *J. Acoust. Soc. Amer.*, vol. 36, no. 6, pp. 1154–1161, 1964.
- [31] L. L. Beranek, *Acoustics*. New York, NY, USA: ASA, 1996.
- [32] D. T. Martin, J. Liu, K. Kadirvel, R. M. Fox, M. Sheplak, and T. Nishida, "A micromachined dual-backplate capacitive microphone for aeroacoustic measurements," *J. Microelectromech. Syst.*, vol. 16, no. 6, pp. 1289–1302, Dec. 2007.
- [33] Z. Skvor, "On the acoustical resistance due to viscous losses in the air gap of electrostatic transducers," *Acustica*, vol. 19, no. 5, pp. 295–297, 1967.
- [34] D. Homentcovschi and R. N. Miles, "Viscous damping of perforated planar micromechanical structures," *Sens. Actuators A, Phys.*, vol. 119, no. 2, pp. 544–552, 2005.
- [35] T. S. Miller, J. M. Gallman, and M. J. Moeller, "Investigation of low-frequency single point wall pressure spectrums," *AIAA2011-2739*, in *Proc. 17th AIAA/CEAS Aeroacoust. Conf.*, Portland, OR, USA, 2011.
- [36] T. Miller, S. Lee, G. Holup, J. M. Gallman, and M. J. Moeller, "Design of a quiet inlet for a 6×6 boundary layer flow duct," SAE Tech. Paper 2011-01-1617, 2011, doi:10.4271/2011-01-1617.
- [37] G. M. Corcos, "Resolution of pressure in turbulence," *J. Acoust. Soc. Amer.*, vol. 35, no. 2, p. 192, 1963.
- [38] M. J. Madou, *Fundamentals of Microfabrication: The Science of Miniaturization*, vol. 6. Boca Raton, FL, USA: CRC Press, 2002.
- [39] Para Tech Coatings Inc. (2014, Mar. 21). *PTC Parylene Properties Chart* [Online]. Available: http://www.parylene.com/pdfs/PTC-Parylene_Properties_Chart.pdf
- [40] M. Gad-el-Hak, *The MEMS Handbook*. Boca Raton, FL, USA: CRC Press, 2002.
- [41] C. Shih, T. A. Harder, and Y.-C. Tai, "Yield strength of thin-film parylene-C," *Microsyst. Technol.*, vol. 10, no. 5, pp. 407–411, 2004.
- [42] D. F. Lemmerhirt, X. Cheng, R. D. White, C. A. Rich, M. Zhang, J. B. Fowlkes, et al., "A 32×32 capacitive micromachined ultrasonic transducer array manufactured in standard CMOS," *IEEE Trans. Ultrason., Ferroelectr., Freq. Control*, vol. 59, no. 7, pp. 1521–1536, Jul. 2012.
- [43] M. J. Walsh, "Riblets as a viscous drag reduction technique," *AIAA J.*, vol. 21, no. 4, pp. 485–486, 1983.
- [44] R. H. Mellen, "On modeling convective turbulence," *J. Acoust. Soc. Amer.*, vol. 88, no. 6, pp. 2891–2893, 1990.
- [45] R. H. Mellen, "Wave-vector filter analysis of turbulent flow," *J. Acoust. Soc. Amer.*, vol. 95, no. 3, pp. 1671–1673, 1994.
- [46] T. S. Miller and M. J. Moeller, "A note on equilibrium turbulent boundary layer wall pressure models," *SAE Int. J. Passenger Cars, Mech. Syst.*, vol. 2, no. 1, pp. 1538–1549, 2009.



Joshua S. Krause received the B.S. degree in integrated science and technology from James Madison University, Harrisonburg, VA, in 2006, and then received M.S. and Ph.D. degrees from Tufts University in 2008 and 2011, respectively.

In 2011, he joined Raytheon Company, Andover, MA, and is Process and Yield Integration Engineer working on research and development for both microelectromechanical systems (MEMS) and microwave gallium nitride (GaN) process development. His expertise is in the design, manufacturing, and characterization of MEMS, as well as the transition to production for emerging semiconductor processes. He is the author of multiple technical publications and has filed for one patent.

Dr. Krause has received multiple Best Poster/Paper Awards from ASME and ASA.



Judith M. Gallman earned the B.S. in aerospace engineering from Parks College, Saint Louis University, and the M.S. in aeronautics from the School of Engineering and Applied Science, The George Washington University, NASA Langley Research Center, Joint Institute for the Advancement of Flight Sciences.

She worked for the U.S Army Aeroflightdynamics Directorate at NASA Ames Research Center as a Research Scientist performing research in helicopter noise from November 1988 until August 1995. She then worked for the National Institute for Aviation Research at Wichita State University where she applied her helicopter noise expertise to general aviation propeller noise as a Research Associate from November 1995 until June 1996. In July of 1996, she joined Boeing Commercial Airplanes in Wichita, Kansas to support nacelle acoustic liner design, test, and manufacturing, and became an Associate Technical Fellow in 2004. Boeing divested the Wichita facility in 2005. At that point, she became the Acoustic Lab Manager to support interior noise for the Boeing 787 program, sonic fatigue, and acoustic analysis for all Spirit AeroSystems built pylons and nacelles. In October of 2013, she joined the Gulfstream Aerospace Corporation, Savannah, Georgia, as a Technical Specialist in Acoustics and Vibration.

Ms. Gallman was appointed as an Associate Technical Fellow by Boeing in 2004. This appointment was honored by Spirit AeroSystems. She is a Senior Member of AIAA, and has published numerous journal articles and meeting papers.



Mark J. Moeller received a B.S. degree in aerospace engineering from Iowa State University in 1976, an S.M. in ocean engineering from MIT in 1977, a Diploma with Honors from the von Karman Institute of Fluid Mechanics in 1978, and a Ph.D. in applied mechanics from MIT in 1982.

He worked on flow induced noise and vibration on a broad spectrum of problems ranging from submarines, cars, and aircraft throughout his career. He is currently retired. He has multiple publications related to flow noise.

Dr. Moeller is a member of the SAE and Sigma XI.



Robert D. White (S'00–M'05) received B.S. and M.S. degrees in mechanical engineering from the Massachusetts Institute of Technology in 1999, and the Ph.D. degree in mechanical engineering from the University of Michigan, Ann Arbor, in 2005.

He worked as a MEMS Test Engineer at the C.S. Draper Laboratories, Cambridge, MA, on MEMS gyroscopes and accelerometers from 1999–2000. In 2005, he joined Tufts University, Medford, MA, as an Assistant Professor of mechanical engineering. In 2011, he was promoted to Associate Professor. His primary research interest is in the design, fabrication, modeling, and testing of microsystems, in particular, acoustic devices and aerodynamic measurement technologies, with additional work in inner ear mechanics, acoustics and vibrations, and mechatronics. He teaches in the areas of microsystems, acoustics, dynamics, and controls. Since 2007, he has directed the Tufts Micro and Nano Fabrication Facility. He is the author of multiple technical publications and patents.

Dr. White received a C.S. Draper Fellowship in 1998, the NSF Graduate Research Fellowship in 2001, a Rackham Predoctoral Fellowship in 2004, and the Tufts Outstanding Contributor to Graduate Education in 2011. He is a member of the ASA, ASME, AIAA, and IEEE.